Studies and Practices of Geosynthetic Reinforced Soil (GRS) Abutments and Integrated Bridge Systems

Chao Xu¹, Qingming Wang¹, and Chongxi Zhao¹, Cheng Liang², Minmin Luo³

(¹ Department of Geotechnical Engineering, College of Civil Engineering, Tongji University, Shanghai, 200092, China. ² Institute of Science and Technology, China Three Gorges Corporation, Beijing 100038, China. ³ The Architectural Design and Research Institute of Zhejiang University Co., Ltd., Hangzhou 310028, China.)

ABSTRACT

Geosynthetic reinforced soil (GRS) structures have been widely used in engineering constructions in the past decades. Particularly, there is a growing application of the GRS structures used to support the bridge load due to their high bearing capacity. In this study, a series of compressive strength tests on GRS composite were conducted, and a more accurate calculated model for the compressive strength was developed. Furthermore, centrifuge model tests were performed to investigate the influence of design parameters (e.g., setback distance and beam seat width) on the ultimate bearing capacity and deformation characteristics of GRS abutments. Based on these findings, a calculation method for the ultimate bearing capacity of GRS abutments considering design parameters was proposed, along with modifications to the method proposed by the Federal Highway Administration (FHWA) guidelines to illustrate the relationship between maximum facing deformation and settlement. Shaking table tests on a whole GRS-IBS demonstrated that the bridge beam significantly affected the dynamic response of the system, while also proving its exceptional resistance to seismic waves. Finally, the applications of GRS-IBS in China were presented through a typical case.

Keywords: Geosynthetics; GRS abutment; GRS-IBS; Model tests; Analytical investigations

1 INTRODUCTION

The reinforced soil technology has been widely used in engineering construction since ancient times. Archaeological evidence reveals that early implementations dating back to Neolithic periods (circa 3000 BCE) incorporated organic composites in hydraulic infrastructure, as exemplified by the Liangzhu Ancient City ruins, where engineers mixed plant fibers with silt for flood control systems. Concurrently, ancient Mesopotamian societies (circa 600 BCE) developed analogous palm-fiber reinforcement methodologies in ziggurat constructions. These innovations demonstrate the superb wisdom of ancient humans in using biomaterials to solve engineering problems. The modern reinforced soil technology emerged during the 1960s when French civil engineer Henri Vidal revolutionized geotechnical practice through his pioneering development of metallic strip-reinforced retaining walls. This innovation rapidly gained attention from the global engineering community. decades witnessed Subsequent substantial progress through continuous material innovation, particularly with the advent of polymeric geosynthetics. Geosynthetic reinforced structures have shown significant advantages in life-cycle cost efficiency and environmental

sustainability, leading to their international adoption in infrastructure construction. So far, through rigorous experimental studies theoretical modeling, the fundamental reinforcement mechanisms of geosynthetic-soil interactions have been clarified, and the design methodologies and analytical frameworks of geosynthetics-reinforced soil structures developed. This progression has established geosynthetics-reinforced soil as a prominent research branch within geotechnical engineering.

Extensive research to date has demonstrated that the reinforcement spacing plays a crucial role in governing the mechanical properties of reinforced soil structures by influencing the interaction range at the soil-reinforcement interface and the stress transfer pathways (Adams et al., 2007b: Palmeira. 2009). Furthermore. revealed that experimental studies reinforcement spacing exerted greater influence on system performance than the reinforcement tensile strength in a reinforced soil mass (Wu et al., 2013; Nicks et al., 2016; Shen et al., 2019). Therefore, the reinforcement spacing is considered an important influencing factor in reinforced soil structures. Currently, researchers have reached distinguishing consensus on geosynthetic

(GRS) reinforced soil from conventional geosynthetic mechanically stabilized earth (GMSE) systems based on reinforcement spacing, with the GRS composed of closely-spaced reinforcement layers of smaller than 30 mm. This close reinforcement spacing enhances soil-geosynthetic interface behavior, leading to high load-bearing capacity and composite behavior with self-stabilization properties (Nicks et al., 2013; Han et al., 2017). Therefore, the traditional GMSE design frameworks are inapplicable to the GRS structures. These findings of GRS provide a strong foundation for its application in infrastructures, particularly in GRS abutments and geosynthetics reinforced soil-integrated bridge systems (GRS-IBS).

Following the pioneering implementation of GRS-IBS technology on Bowman Road in Ohio in 2005, the U.S. Federal Highway Administration (FHWA) began to promote this rapid-construction bridge technology and considered the GRS-IBS bridge construction technology as part of the "Bridge of the Future" program (Adams et al., 2007a). In 2012, the FHWA reported the "Geosynthetic Reinforced Soil Integrated Bridge System Interim Implementation Guide", which significantly accelerated the adoption of the GRS-IBS bridge technology (Adams et al., 2011). This manual was revised in 2018, and the new vision manual provided more information on the design and construction of GRS abutments and the GRS-IBS (Adams and Nicks, 2018).

Up to now, although great advancements have been made on GRS mass and GRS abutments, and numerous engineering cases of GRS-IBS have been constructed and monitored around the world, there are still some critical problems about the GRS technology that need to be addressed. These problems could be summarized as follows: (1) Material limitations: current compressive strength models for GRS masses inadequately address non-gravel backfill materials, restricting sustainable material alternatives in abutment construction. (2) The **FHWA** auidelines recommended using the compressive strength of GRS mass to evaluate the bearing capacity of GRS abutments directly, which neglected critical boundary condition variations and the influence of design parameters of the GRS abutment, such as the setback distances and beam seat width. (3) Current deformation mechanism of the GRS abutment remains incomplete, especially the relationship between the maximum lateral facing displacement and settlement at the top of the abutment, which has significant uncertainty. (4) The dynamic response characteristics and seismic performance of the whole GRS-IBS need

comprehensive validation through shaking table tests. Building upon the continuous research on the soil-reinforcement interaction mechanism and the GRS structures since 2003, our research team achieved a series of findings. Therefore, based on the aforementioned problems and combined with the 10-year research on GRS structures of our team, this paper systematically presents the findings on GRS mass, GRS abutments, and GRS-IBS structures through a series of experimental studies and theoretical explorations. Finally, the applications of GRS-IBS in China are also illustrated.

2 COMPRESSIVE STRENGTH OF GRS MASS

2.1 Plane strain tests of GRS mass

The GRS abutment directly supports the bridge load, which is quite different from the traditional retaining structure with no loads or small uniform loads applied on its top surface. Therefore, the bearing capacity of the GRS abutment is important for its service performance. Researchers have conducted large-scale model tests to investigate the compressive strength of GRS mass with different influencing factors and boundary conditions (Elton and Patawaran, 2004; Adams et al, 2007b; Pham, 2009). In addition, Yang (1972) and Wu and Pham (2013) proposed analytical methods to predict the compressive strength of GRS, respectively. The Yang method assumed that the reinforcement spacing had the same effect as the reinforcement stiffness on the compressive strength, which meant that a decrease in reinforcement spacing had the same effect as a proportional increase in reinforcement strength. However, this assumption was proven unreasonable by Wu and Pham (2013), who found that the compressive strength of the GRS mass was strongly affected by reinforcement spacing and the influence of reinforcement strength was less significant. They proposed a semi-empirical equation to predict the compressive strength for closely-spaced reinforced soil incorporating a dimensionless W factor. This parameter quantitatively accounted for both reinforcement spacing effects and maximum particle diameter of the backfill soil. It should be pointed out that the Wu and Pham method was validated through a series of model tests with the maximum particle diameter larger than 10 mm. In other words, this method was unsuitable when the maximum particle diameter was smaller than 10 mm. In most current GRS abutment cases, the diameter range of the backfill soil was strictly limited to 12.7 mm to 50 mm. These constraints are not conducive to economic utilization of locally available soils in

certain regions, potentially hindering the promotion and application of the GRS abutment. Further research is needed to verify whether this analytical method is applicable for the GRS with other particle diameters of the backfill soil, especially for sand.

Therefore, a series of plane-strain tests were conducted to evaluate the compressive strength of GRS mass using the backfill soil with a maximum particle size of less than 3 mm. The dimensions of the GRS mass constructed in this study were 600 mm(length)×285 mm(width)×1000 mm(height), as illustrated in the test configuration shown in Fig. 1. Lateral confinement during construction and loading stages was achieved through two air bags located at the left and right side of the GRS mass. During the construction of the GRS mass, a constant confining pressure of 90 kPa was maintained to establish boundary conditions simulating rigid lateral constraints, thereby effectively restraining soil deformation. pressure level was subsequently reduced to 30 kPa after the construction, representing the theoretical lateral earth pressure at mid-depth of a prototype 7 m GRS wall. The reduced confinement pressure remained constant during the subsequent loading process.

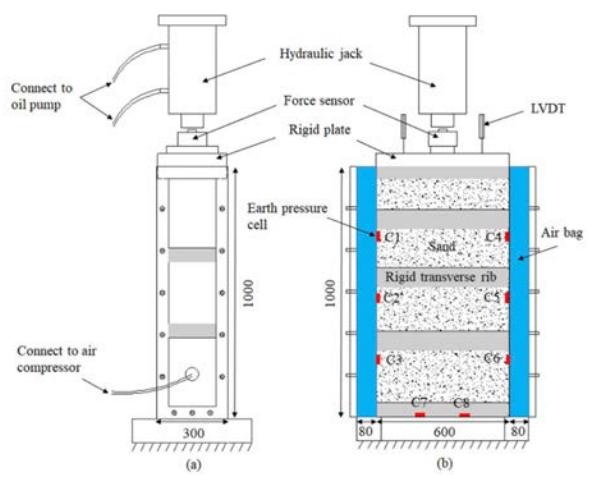


Fig.1. Layout of the test setup: (a) Side view; (b) Front view (Unit: mm)

The test plan was shown in Table 1. A total of 13 plane-strain tests were designed and conducted to investigate the effects of backfill soil gradation, reinforcement strength, and reinforcement spacing on the compressive strength of GRS mass. Dry silicon sand with three different gradations was chosen as backfill soil. Fig. 2 shows the particle size gradation curve of the backfill soil. Notably, the three different gradations of backfill had the same maximum and minimum particle diameter size. The maximum particle size of 3 mm was much smaller than that used in the laboratory tests

conducted by Pham (2009). Triaxial tests revealed that the internal frictions were 39°, 35°, and 42° for G1, G2, and G3, respectively. Two types of biaxial polypropylene (PP) geogrids were chosen as the reinforcement material. The ultimate tensile strengths of the geogrids were 20 kN/m and 30 kN/m for G-20 and G-30 through wide-width tensile tests. The tensile strengths at 2% tensile strain of G-20 and G-30 were 7.6 kN/m and 9.4 kN/m, respectively.

Table 1. Test plan

Test No.	Gradation	Reinforcement	Reinforcement
		strength T_f (kN/m)	spacing $S_{\nu}(kN/m)$
T1	G1	20	0.33
T2			0.25
T3			0.20
T4		30	0.33
T5			0.25
T6		Unreinforced	/
T7	G2	20	0.20
T8			0.25
T9		30	0.25
T10		Unreinforced	/
T11	G3	20	0.25
T12		30	0.25
T13		Unreinforced	/

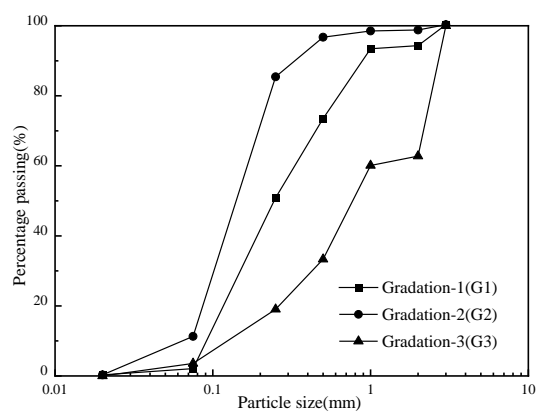


Fig.2. Particle size gradation curve of the backfill soil

In order to capture the load-deformation response, the GRS mass was vertically loaded in stages with a stress increment of 25 kPa. Each stage was maintained for 10 min until the deformation of the model became stable. The loading was terminated when the vertical deformation of the model was not stable, or the deformation rate increased rapidly during load application. The detailed process of the tests could be found in the published paper of Xu et al. (2019).

Fig. 3 illustrates the normalized load-deformation responses of the GRS mass with different influencing factors. The normalized settlement was expressed as the ratio of vertical displacements at the top of the GRS mass to its height. Obviously, the compressive strength of the

unreinforced soil had the minimum value compared to that of the GRS mass. Under constant G1 gradation, the compressive strength increased 19% when reinforcement strength increased from G-20 to G-30. The compressive strength decreased with increasing reinforcement spacing, as shown in Fig.3 (a). In addition, the compressive strength was significantly affected by the backfill soil gradation. G3 with a friction angle of 42° had the largest compressive strength, while G2 had the smallest compressive strength since G2 had the lowest friction angle of 35° among all three gradations.

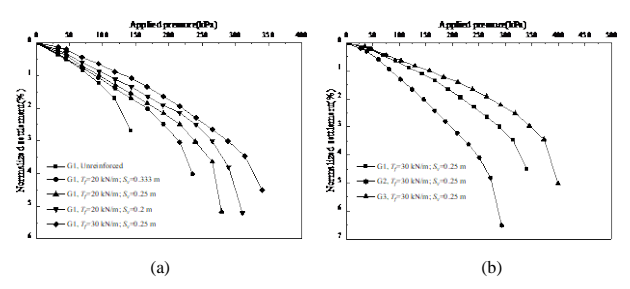


Fig.3. Load-deformation curves of the GRS mass: (a) effects of reinforcement strength and spacing; (b) effects of backfill soil gradation.

As illustrated before, Wu and Pham (2013) proposed an analytical method to predict the compressive strength of GRS mass. This method could be described using Eq. (1):

$$\delta_{\rm I} = \left(\delta_3 + 0.7^{\left(\frac{S_{\nu}}{S_{ref}}\right)} \frac{T_f}{S_{\nu}}\right) K_p + 2c\sqrt{K_p} \tag{1}$$

where δ_1 is the compressive strength of GRS mass; δ_3 is the applied confining pressure; S_V is the reinforcement spacing; S_{ref} is the reference spacing and can be expressed alternatively as $6d_{max}$ or $20d_{85}$; d_{max} is the maximum particle size of backfill soil, d_{85} is the equivalent particle diameter for which 85% of the soil by weight is finer; T_f is the ultimate tensile strength of reinforcement, K_P is the coefficient of passive earth pressure, c is the backfill soil cohesion, when the backfill soil is sand or gravel, c is considered as 0 kPa.

In order to verify whether the Wu and Pham method are applicable to the GRS mass with the backfill of sand, a comparison between the calculated compressive strength using Eq. (1) and the measured values in the tests, as shown in Fig. 4. It could be found obviously that the Wu and Pham method significantly underestimated the compressive strength of the GRS. In addition, Eq. (1) considered the effect of the backfill soil gradation through d_{max} or d_{85} . The d_{max} was the same for all three gradations of sand, while the d_{85} had different values. Fig. 4 shows that the

calculated compressive strengths of the GRS mass using d_{max} and d_{85} were almost the same. Moreover, the calculated values increased with the increasing internal friction angle of the backfill soil, but they did not change much with the variation of reinforcement spacing and reinforcement strength. Therefore, this analytical method needs to be further improved to have more accurate prediction accuracy.

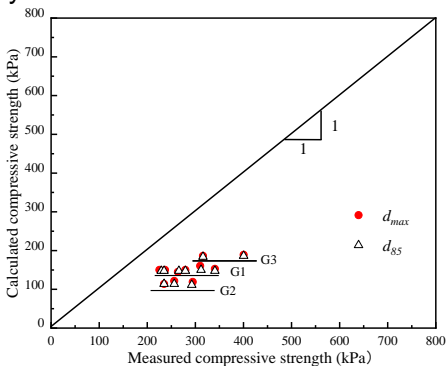


Fig. 4. Comparison between the measured ultimate bearing capacity of the GRS mass and calculated values

2.2 Improved method for calculating the compressive strength of GRS mass

In the Wu and Pham method, the increased confining pressure in soil due to the presence of reinforcement was expressed as:

$$\delta_3 = W \frac{T_f}{S_y} \tag{2}$$

Where *W* is used to represent the contribution of the reinforcement to the compressive strength of the GRS mass.

The W factor is an exponential function with a base of 0.7 and the ratio of reinforcement spacing to the maximum particle size of the backfill soil (S/d_{max}) as the independent variable. In order to investigate the influence of the W factor on the compressive strength of GRS mass, the data collected from published literature, as listed in Table 2, were used to further study. The relationships between the S_{ν}/d_{max} and the ratio of the measured and calculated compressive strength using the data of GRS mass tests from table 2, were shown in Fig. 5. It could be found that when $S_{V}/d_{max}>25$, the calculated compressive strengths were smaller than the measured values, indicating that calculated method proposed by Wu and Pham (2013) underestimated the compressive strength of GRS mass. On the contrary, when the S/d_{max} <10, the calculated compressive strengths were obviously greater than the measured values, indicating that the calculated method overestimated the compressive strength of GRS mass. Therefore, the W factor was expressed using a segmented equation based on the value of S/d_{max} . it should be pointed out that in order to

simplify the calculation method, the coefficients of S/d_{max} were obtained by fitting the data from Table 2. The modified W using the parameter of d_{max} could be expressed as follows:

Table 2 Data sources

Literature	Test number	Test method
Adams et al., 2007b	5	Mini-pier test
Nicks et al., 2013	19	Mini-pier test
		Generic soil
Wu et al., 2013	5	geosynthetic composite
		(GSGC) test
Elton and	7	Unconfined compression
Patawaran, 2004	,	test
Ruiken et al., 2011	7	Large-scale triaxial test
This study	13	Plane-strain test

$$W = \begin{cases} 0.7^{(S_{v}/3d_{\text{max}})}, & S_{v}/d_{\text{max}} < 10\\ 0.7^{(S_{v}/6d_{\text{max}})}, & 10 \le S_{v}/d_{\text{max}} \le 25\\ 0.7^{(S_{v}/40d_{\text{max}})}, & S_{v}/d_{\text{max}} > 25 \end{cases}$$
(3)

The modified equation of the W factor using the parameter of d_{85} can be expressed as follows:

$$W = \begin{cases} 0.7^{(S_{v}/6d_{85})}, & S_{v}/d_{\text{max}} < 10\\ 0.7^{(S_{v}/200d_{85})}, & 10 \le S_{v}/d_{\text{max}} \le 25\\ 0.7^{(S_{v}/200d_{85})}, & S_{v}/d_{\text{max}} > 25 \end{cases}$$
(4)

Therefore, the improved method to calculate the compressive strength of GRS mass can be obtained by substituting Eq. 3 and 4 into Eq. 5

$$\delta_1 = \left(\delta_3 + W \frac{T_f}{S_v}\right) K_p + 2c\sqrt{K_p}$$
 (5)

The measured data from the plane-strain tests conducted in this study and the published literature listed in Table 2, were used to validate the accuracy of the improved method proposed in this study, as shown in Fig. 6. It can be seen that the Wu and Pham method presents larger deviations of the compressive strength of GRS mass than the improved method proposed in this study, indicating the improved method provides better predictions of the compressive strength relative to the Wu and Pham method.

It should be noted that the improved method is a semi-empirical method, which is derived from the Wu and Pham method and combined with the experimental data from the published literature of GRS mass. While this improved method demonstrates enhanced predictive performance in the current analysis, its broader applicability needs further verification and exploration.

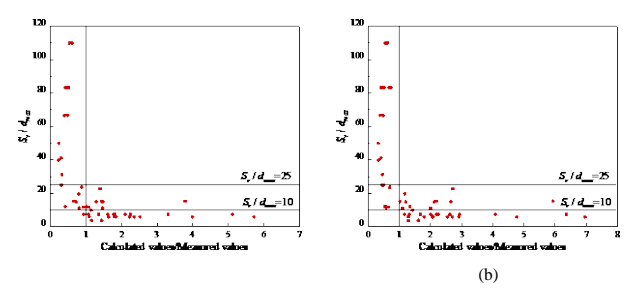


Fig.5. Relationship between the S_v/d_{max} and the ratio between the calculated bearing capacity and the measured values: (a) using the parameter of d_{max} ; (b) using the parameter of d_{85}

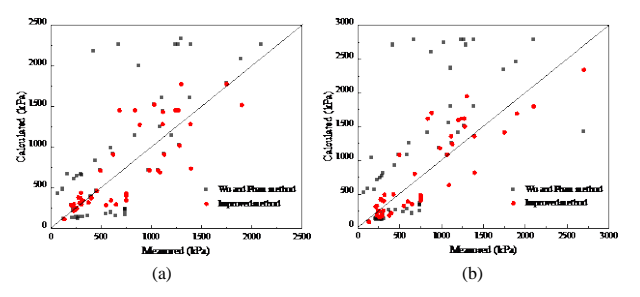


Fig. 6. Comparison between the Wu and Pham method, and the improved method: (a) using the parameter of d_{max} ; (b) using the parameter of d_{85}

3 ULTIMATE BEARING CAPACITY OF GRS ABUTMENT

3.1 Centrifuge model tests

Accurate prediction of ultimate capacity is critical for the design of the GRS abutment. Current FHWA guidelines recommend using Eq. (1), originally developed by Wu and Pham (2013) for GRS mass, to estimate the ultimate bearing capacity of GRS abutment. However, this equation fails to account for structural and boundary condition differences between GRS mass and GRS abutments, particularly neglecting the influence of key design elements such as setback distance and beam seat width in GRS abutments or GRS-IBS. A series of scaled-model tests and numerical simulations of the GRS abutments had proved that the setback distance and the beam seat width had a significant influence on the bearing performance of the GRS abutment (Xiao et al., 2016; Ambauen et al., 2016; Zheng and Fox, 2017; Zheng et al., 2018; Zhang et al., 2020). Therefore, the direct application of Eq. (1) to calculate the ultimate bearing capacity of the GRS abutment is unreasonable. It should be noted that current studies were limited by experimental conditions or simulation software, making them incapable of loading the GRS abutment to a failure state. So, the ultimate bearing capacity and failure modes are inadequately characterized.

To address these limitations, five centrifuge model tests were conducted to investigate the

ultimate bearing capacity and failure modes of the GRS abutments. The geometric prototype of the centrifuge models was based on the Bowman Road Bridge in Ohio, US (Adams et al., 2007). Considering the height of the Bowman Bridge abutment and the dimensions of the model box, the scaling factor N was chosen as 10, with the centrifugal acceleration of the tests of 10g. Fig. 7 illustrates the cross-section details of the abutment model. The geotextile and clean river sand were chosen as the reinforcement material and the backfill soil, respectively. The test plan was shown in Table 3. T1 was set as the baseline group with reinforcement properties strictly scaled from the prototype reinforcement. To circumvent the limitations of the loading apparatus in getting the structural failure state, tests T2 to T5 employed low strenath reinforcements, parametric analysis of setback distance and beam seat width effects on the ultimate bearing capacity of GRS abutments.

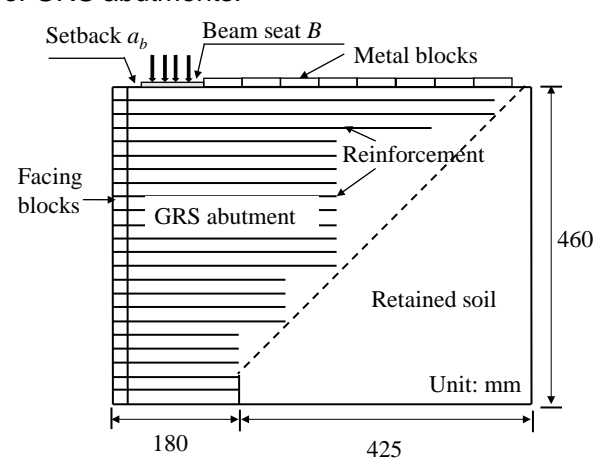


Fig. 7. Schematic of the model GRS abutment (Unit: mm)

Table 3 Test plan for the centrifuge model tests

Test No.	Tensile strength Tf (kN/m)	Setback distance, a _b (mm)	Beam seat width, B (mm)
T1	8.4	20	90
T2		20	90
T3	2.4	40	90
T4	۷.٦	80	90
T5		20	150

Prior to loading, the constructed model was mounted to the centrifuge swing basket. The centrifuge was then accelerated to 10g and maintained at this level until the sensor readings were stable. Subsequently, multi-stage loading was applied through an electric jack with a load cell. The loading stage was terminated when the GRS abutment model failed with excessive deformation or visual collapse. The load recorded before abutment failure was considered as the ultimate

bearing capacity. For the abutment model that had not failed, the loading was terminated before the electric jack reached its maximum output.

Fig. 8 shows the load-vertical relationships for all five GRS abutments. The baseline model (T1) presented stable behavior under loading, with vertical settlement increasing approximately linearly until reaching the maximum loading capacity of 1350 kPa for the loading device. In contrast, significant failure phenomena were observed in tests T2 to T5, where reduced reinforcement tensile strength led to nonlinear strain development and abrupt bearing capacity loss. This contrast indicated the important role of reinforcement strength in governing ultimate bearing capacity. Table 4 shows the ultimate bearing capacity for all five tests and the calculated values using Eq. (1) recommended by the FHWA. Comparing the test results of T2, T3, and T4, it could be found that increasing the setback distance significantly improved the ultimate bearing capacity. But there existed an optimum setback distance, and increasing the setback distance beyond the optimum value had a minor influence on increasing the ultimate bearing capacity. Comparing the results of T2 and T5, the ultimate bearing capacity of the GRS abutment decreased significantly with the increase of the beam seat width. Table 4 also shows that the influence of abutment geometric characteristics (e.g., setback distance and beam seat width) was not considered in this calculated method, resulting in the same calculated values in T2 to T5. In addition, the calculated method proposed by the FHWA significantly underestimated the ultimate bearing capacity of the GRS abutment.

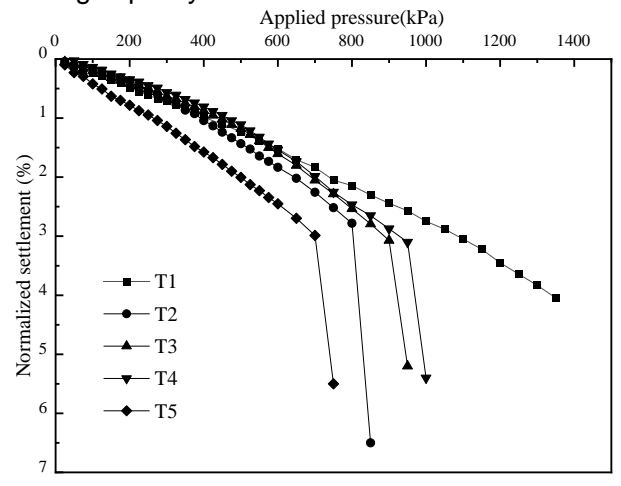


Fig. 8. Load-vertical strain curves of the beam seat

Table 4 Ultimate bearing capacity of GRS abutments

and the committee of the control of				
Test No.	Test results from centrifuge model tests (kPa)	Calculated results using the FHWA method (kPa)		
T1	>1 350	962		

T2	800	
T3	900	233
T4	950	233
T5	700	

3.2 Failure mode analysis

Post-test disassembly of the GRS abutment models revealed critical insights into failure mechanisms. Reinforcements were carefully taken out layer by layer to reconstruct the failure surfaces. The failure surfaces were plotted in Fig. 9, as well as the assumed failure surface proposed by FHWA (Adams and Nicks, 2018), Berg et al. (2009), and Zheng et al. (2018). It could be seen clearly that the failure surface of the GRS abutment observed from the tests originated at the rear edge of the beam seat, propagating downward at a certain angle to the connection between the facing block and the reinforcement. All failure surfaces terminated at approximately the middle height (0.5H) of the abutment, which was quite different from the previous assumptions that the rupture surface terminated at the toe of the wall facing proposed by Berg et al. (2009) and Zheng et al. (2018). Fig. 10 further corroborates these findings through the ruptured reinforcement layers from T2.

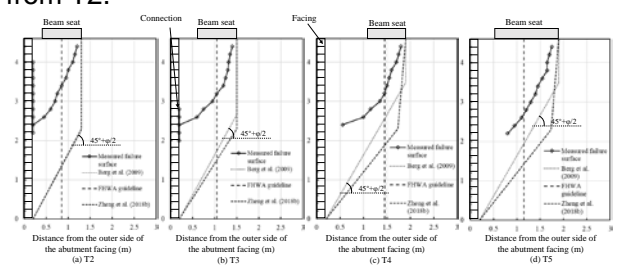


Fig. 9. Failure surface found through centrifuge model tests and predicted potential failure surface: (a) T2: a_b =20mm, B=90 mm; (b)T3: a_b =40mm, B=90 mm; (c) T4: a_b =80mm, B=90 mm; (d) T5: a_b =20mm, B=150 mm

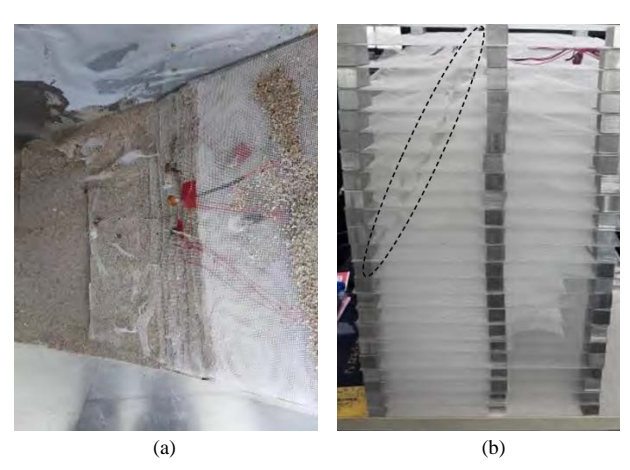


Fig. 10. The failure surface of the reinforcement obtained from T2: (a) Top view after the test; (b) front view of the restored reinforcement failure surface

3.3 Improved method for the ultimate bearing capacity of the GRS abutment

In order to further develop the calculation model of the ultimate bearing capacity for GRS abutments, a bilinear failure surface was proposed based on the findings obtained from the centrifuge model tests. It was assumed that the failure surface started from the rear edge of the beam seat, developing downwards at a horizontal angle of θ_1 and intersecting with the middle surface of the beam seat, and then further developing downwards at a horizontal angle of θ_2 . Finally, the failure surface slides out from the wall face, as depicted in Fig.11.

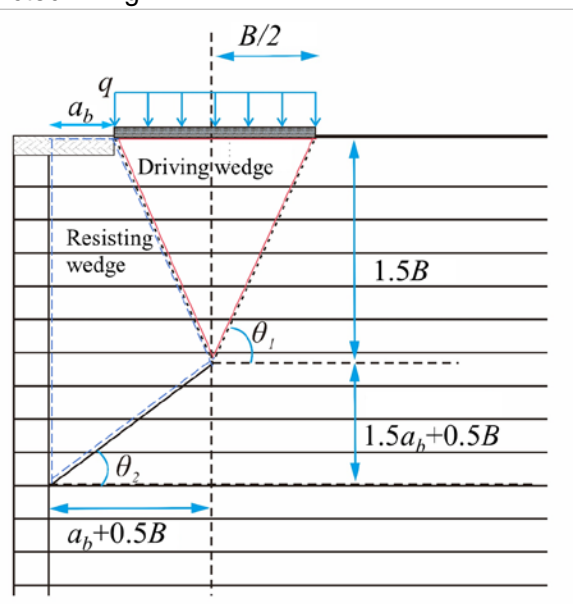


Fig. 11. Driving and resisting wedges for the two-part wedge mechanism

According to the general form of the bilinear failure surface, as shown in Fig. 11, the two-part wedge mechanism is suitable for illustrating the limit state of the GRS abutment, with the turning point of the failure surface to the outer edge of the bearing area. This line is set as the boundary between the driving and resisting wedges (Leshchinsky, 2014; Mirmoradi and Ehrlich, 2018). The driving wedge is an isosceles triangular reinforcement mass enclosed within the bearing area, failure surface, and boundary between the driving and resisting wedges, while the passive wedge is a reinforcement mass enclosed within the failure surface, abutment facing, and the boundary between the driving and resisting wedges. Fig. 12 shows the force analysis of driving and resisting wedges. It should be noted that all the bridge loads are applied on the top of the driving wedge. Therefore, the beam seat or girder fixed in the horizontal direction will apply friction horizontally towards the inner side of the abutment. In this model, the friction force f acting on the abutment applied by the girder or beam seat is taken into consideration. This friction force f is assumed to be uniformly distributed on the bearing area, and can be expressed as: f = n q, where n is the horizontal friction coefficient.

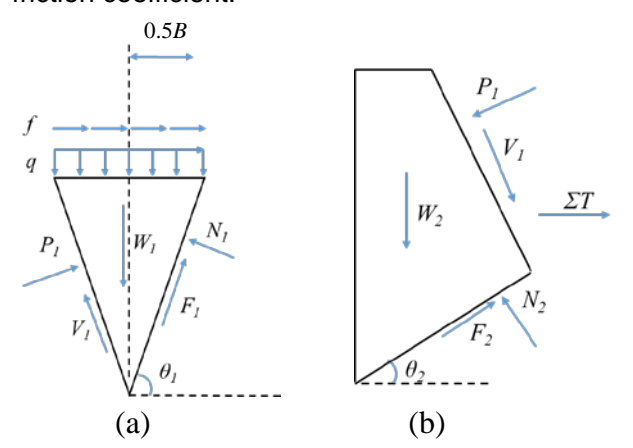


Fig. 12. Forces for the driving and resisting wedge: (a) driving wedge; (b) resisting wedge

The forces for the driving wedge are shown in Fig.12 (a). Among these forces, P_1 is the interwedge normal force; V_1 is the interwedge shear force; W_1 is the self-weight of the driving wedge; N_1 is the normal force acting on the failure surface; F_1 is the frictional force acting on the failure surface. The reinforcement tensile force can be omitted in the driving wedge force analysis process based on the assumption that the reinforcement tensile forces acting on the left and right sides of the driving wedge are the same and opposite in direction.

Using the force equilibrium of the driving wedge, the interwedge normal force P_1 can be determined as follows:

$$P_{1} = \frac{W_{1} + Q_{1} - A_{1}B_{1}Q_{2}}{A_{1}B_{1}(\sin\theta_{1} - \lambda\tan\varphi\cos\theta_{1}) + (\cos\theta_{1} + \lambda\tan\varphi\sin\theta_{1})}$$
(6)

where Q_1 is the total surcharge load applied on abutment, $Q_1=q$ B; Q_2 is the total friction act on the abutment, $Q_2=f$ B; λ is the mobilized coefficient of interwedge shear strength, and the term λ is assumed to 1 due to the driving wedge has a more obvious settlement trend compared to the resisting wedge, and it can be assumed that the shear strength of the backfill between the wedges can be fully mobilized; and the A_1 and B_1 are defined as:

$$A_{\rm l} = \frac{1}{\sin \theta_{\rm l} - \tan \varphi \cos \theta_{\rm l}} \tag{7}$$

$$B_1 = \cos \theta_1 + \tan \varphi \sin \theta_1 \tag{8}$$

The forces for the resisting wedge are shown in Fig.12 (b). The interwedge normal force P_1 can be determined based on the force equilibrium of the resisting wedge, as follows:

$$P_{1}(\frac{1}{A_{3}} - B_{3}A_{2}B_{2}) = A_{2}B_{2}W_{2} + \sum T$$
 (9)

where W_2 is the self-weight of the resisting wedge; ΣT is the sum of the tensile forces of the reinforcement crossing the failure surface. Due to the assumption that the reinforcement tensile forces acting on the left and right sides of the driving wedge are the same and opposite in direction, the reinforcement tensile force acting on the driving wedge is transferred to the analysis of the resisting wedge. Hence, ΣT includes the tensile force of all reinforcement crossing the failure surface. θ_2 is the angle between the lower half of the failure surface and the horizontal direction. A_2 , B_2 , A_3 and B_3 can be expressed as follows:

$$A_2 = \frac{1}{\cos \theta_2 + \tan \varphi \sin \theta_2}$$
 (10)

$$B_2 = \cos \theta_2 \tan \varphi - \sin \theta_2 \tag{11}$$

$$B_2 = \cos \theta_2 \tan \varphi - \sin \theta_2$$

$$A_3 = \frac{1}{\sin \theta_1 - \lambda \tan \varphi \cos \theta_1}$$
(11)

$$B_3 = \cos \theta_1 + \sin \theta_1 \lambda \tan \varphi \tag{13}$$

Combining the equations, the ultimate bearing capacity *q* can be calculated as:

$$q = \frac{(A_1B_1 + A_3B_3)(A_2B_2W_2 + \sum T)}{(1 - A_2B_2A_3B_3)} - W_1}{(1 - A_1B_1n)B}$$
(14)

Considering that the rupture reinforcement first occurred on a certain layer, and the other layers of reinforcement subsequently ruptured along the failure surface according to the centrifugal model test results, hence, the mobilized tensile strength of each reinforcement layer should be confirmed. Referring to the method of the W factor in Eq. (1) and introducing the exponential form of the reinforcement coefficient, expression of $\sum T$ can be assumed as follows:

$$\sum T = N(0.7^{\frac{S_{\nu}}{6d_{\text{max}}}} T_f)$$
 (15)

Where N is the number of reinforcement layers that cross the failure surface; d_{max} is the maximum particle size of the backfill; T_f is the ultimate tensile strength of the reinforcement.

In order to confirm the value of the horizontal friction coefficient n, the results of the centrifuge tests T1-T5 were used to determine the value of n by inverse calculation. The inverse calculation result shows that n is between 0.273 to 0.303. Conservatively, n is chosen as 0.273 in this proposed model.

Fig.13 shows the comparison between the calculated ultimate bearing capacity using the proposed method and the measured values from centrifuge model tests. Obviously, the measured and calculated ultimate bearing capacity are near the 1:1 line, indicating that this proposed method

can accurately evaluate the ultimate bearing capacity of GRS abutments. That is because the proposed method considers the actual failure surface of the GRS abutment and takes into account the influence of the setback distance and beam seat width on the ultimate bearing capacity.

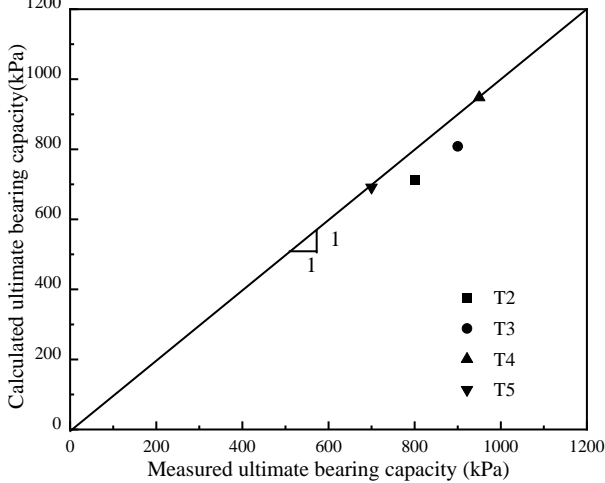


Fig. 13. Comparison between the measured ultimate bearing capacity of the centrifuge model tests and the calculated values using the proposed method

4 DEFORMATION CHARACTERISTICS OF GRS ABUTMENTS

4.1 Deformation characteristics of GRS abutments from centrifuge model tests

Compared to the ultimate bearing capacities, the deformation characteristics of the GRS abutment are equally important to its working performance under service load conditions. A series of studies have shown that different influencing factors have different effects on lateral facing displacements and settlements at the top of the GRS abutment, such as the vertical spacing, backfill soil, reinforcement length, reinforcement stiffness, setback distance, beam seat width, abutment height, and loading conditions (Ambauen et al., 2015; Abu-Farsakh er al., 2018; Zheng et al., 2019; Shen et al., 2020). It should be pointed out that due to the existence of the free-standing facing of the GRS abutment, the lateral facing displacement and the settlement at the top of the abutment are highly related. It is necessary to correlate both the lateral and the vertical deformations when analyzing the deformation characteristics of the GRS abutments. In the current FHWA design and construction guidelines, the relationship between the maximum lateral facing displacement of the GRS abutment and the maximum settlement at the top of the abutment was proposed as follows:

$$D_L = \frac{2b_q}{H}D_{\nu} \tag{16}$$

Where D_L is the maximum lateral facing displacement; D_V is the maximum settlement at the top of the abutment; b_q is the width of the load area along the top of the abutment, including the setback distance ($b_q=a_b+B$), and H is the abutment height.

However, Saghebfar et al. (2017) and Khosrojerdi et al. (2020) found that the calculated results using the FHWA method significantly underpredicted the maximum lateral facing displacements through field instrumentation and numerical simulations, and more attention should be paid to this calculated method. Fig.14 shows the assumed deformation distribution of GRS abutment under vertical loading in the FHWA Α uniform distribution of vertical deformation occurs at the top of the GRS abutments, and a triangular distribution of lateral deformation occurs along the abutment height. This assumption means that the settlement at the setback distance and the beam seat width are the same, and the settlement that occurred at the roadway approach can be ignored. In addition, zero-volume change of the GRS abutments and a composite behavior with the reinforcement layers and the backfill deformed laterally together are also assumed.

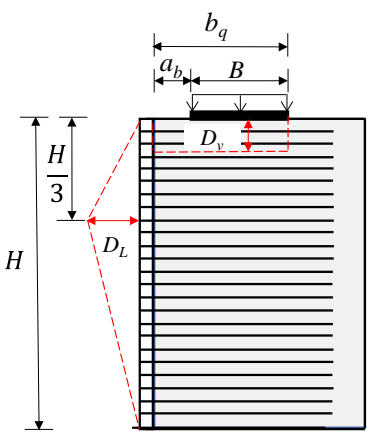


Fig.14. Illustration of the deformed GRS abutment assumed by the FHWA method.

Previous studies have shown that when highly compacted backfill soil and closely spaced reinforcement were used, it can be considered that the GRS structure has a composite behavior (Wu et al., 2006; Nicks et al., 2013). However, the settlement at the range of setback distance and the beam seat width may be quite different. It cannot be simply assumed that a uniform settlement occurs at the top of the abutment. The authors conducted five centrifuge model tests to investigate the influence of setback distance and beam seat width on the deformation characteristics of GRS abutment through simulating a 6 m high abutment. The results showed that most of the

settlements were concentrated under the beam seat, with smaller settlements occurring under the setback area and the approach roadway. The test results also showed that the facing deformation was guite irregular. In addition, the assumption of zero-volume change was also proved suitable for the deformation calculation of the GRS abutments. Fig.15 shows the relationship between maximum lateral facing displacements and the maximum settlements at the top of the abutments measured in the tests. It can be seen that the maximum lateral facing displacements increased approximately linearly with the increase of the maximum settlements. And the slopes of the fitting lines were different under different a_b and B, indicating that the setback distance and beam seat width had different effects on the relationship between the maximum lateral displacements and the maximum settlements at the top of the GRS abutments. Therefore, these two influencing factors should be separately considered when calculating the deformation of the GRS abutment.

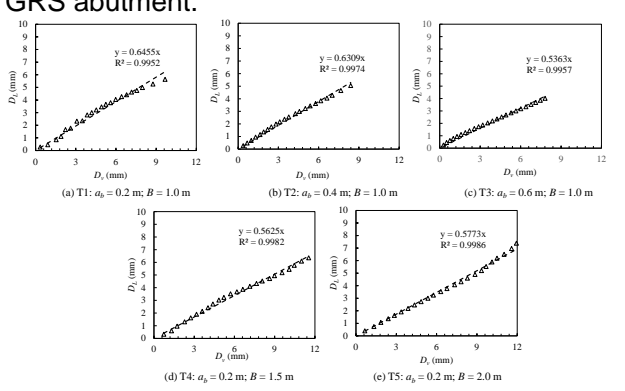


Fig. 15 Relationships between the maximum lateral facing displacements and the maximum settlements at the top of the abutments: (a) T1: $a_b = 0.2$ m; B = 1.0 m (b) T2: $a_b = 0.4$ m; B = 1.0 m; (c) T3: $a_b = 0.6$ m; B = 1.0 m; (d) T4: $a_b = 0.2$ m; B = 1.5 m; (e)T5: $a_b = 0.2$ m; B = 2.0 m.

4.2 Improved method for the deformation calculation of the GRS abutment

According to the centrifuge model test results, zero-volume change was also assumed in the improved method. Different from the deformation distribution of the GRS abutment assumed in the settlement **FHWA** method, а trapezoidal distribution was assumed in the improved method with a uniform distribution under the beam seat and two triangular settlement distributions under the setback area and the approach roadway, as shown in Fig. 16. Due to the irregular distribution of the lateral facing displacement, the improved method used an equivalent rectangular distribution located at the mid to top portion of the abutment to describe irregular distribution along the whole abutment height for simplification. Therefore, the area of the assumed rectangle is equal to the actual irregular area. The adjustment parameter k was determined under different vertical loads in all five centrifuge model tests. An average value of 2.2 was selected in the improved method. The detailed calculation and verification process of the assumed deformation distribution can be founded in Wang et al. (2024). Therefore, based on the zero-volume change assumption and the modified distributions of both the vertical and the lateral deformations, the improved method to describe the relationship between the maximum lateral facing displacements and the maximum settlements at the top of the GRS abutments can be expressed as:

$$D_L = \frac{0.5a_b + 1.5B}{2.2(a_b + B)} D_{\nu}$$
 (17)

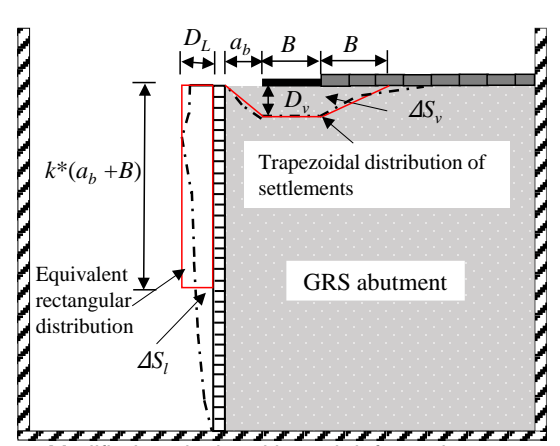


Fig. 16 Modified vertical and lateral deformation distributions of the GRS abutments

Fig. 17 shows the comparison between the measured and calculated maximum lateral facing displacements the improved using proposed in this study. The calculated maximum lateral facing displacements matched well with the measured values, indicating that the improved method could be used to reasonably describe the relationship between the maximum lateral facing displacements and the maximum settlements at the top of the GRS abutments with different setback distances and the beam seat widths. In addition, the data from the published literature were also used to further validate the accuracy of the improved method, as shown in Fig. 18. It can be seen that the FHWA method had larger deviations of the calculated maximum lateral facing displacements than the improved method. indicating that the improved method gave better predictions of the abutment deformations than the FHWA method. Therefore, it can be concluded that the improved method could significantly improve the prediction accuracy of the deformations of the GRS abutments induced by vertical loads.

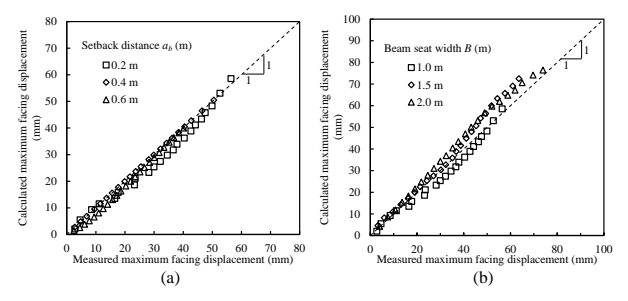


Fig. 17. Validation of the improved method using the centrifuge test results: (a) effects of the setback distance a_b with B = 1.0 m; (b) effects of the beam seat width B with $a_b = 0.2$ m.

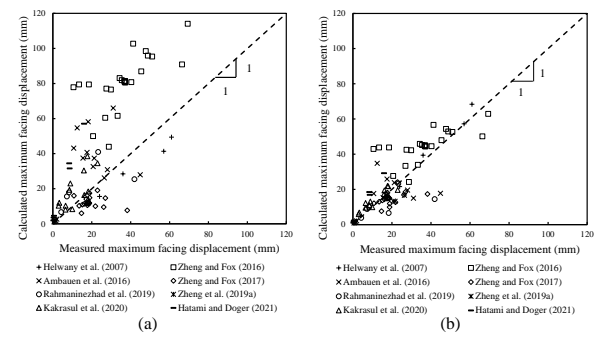


Fig. 18 Comparison between the results published in literature and the calculated maximum lateral facing displacements using: (a) the FHWA method, and (b) the improved method

5 SEISMIC PERFORMANCES OF THE GRS-IBS

Over the past few decades, the GRS structures have presented excellent seismic performance based on scientific research results and post-earthquake investigations. The seismic performances of the GRS abutments were also investigated by some researchers (Helwany et al., 2012; Zheng et al., 2019; Askari et al., 2021). These investigations have shown that the GRS abutments also had overall good seismic performance in terms of lateral displacements and bridge beam seat movements. However, it should be noted that the reported investigations just focused on the seismic behavior of a single abutment with a segment of the bridge beam resting on its top, with the other end of the bridge beam resting on a rigid support wall with rollers or a sliding platform. Therefore, these studies may not truly reflect the conditions of the whole GRS-IBS constructed in the field. It is necessary to conduct shaking table tests on the whole GRS-IBS to evaluate the effect of the bridge beam on both GRS abutments.

5.1 Shaking table test of a whole GRS-IBS

The Guthrie Run bridge, constructed in Delaware, US, was selected as the prototype case

with a typical height of 6 m (Talebi, 2016). Considering the geometry and the payload of the shaking table, a length scaling factor of 4 was adopted in this study. The model GRS-IBS consisted of two GRS abutments at opposite ends and a full-length bridge beam resting on the top of the two abutments. The total height of the model was 1.5 m, consisting of a 1.2 m high abutment, a 0.15 m thick reinforced soil foundation (RSF), and a 0.15m thick approach roadway. Fig. 19 and Fig. 20 show the configuration geometry and the constructed model of the GRS-IBS, respectively. detailed model descriptions and the construction process of the GRS-IBS can refer to Xu et al (2020). Poorly-graded guartz sand with a peak friction angle of 49° and a biaxial geogrid were used as the backfill soil and reinforcement material, respectively. Table 5 shows the shaking table test plan. Two sets of shaking table tests were conducted to investigate the effect of reinforcement spacing and length on the seismic performance of GRS-IBS under the same ratio of reinforcement strength to reinforcement spacing. Therefore, two biaxial geogrids with different tensile strengths were used in the two GRS abutments at opposite ends. The geogrids were mechanically connected with the facing blocks by inserting steel wires through the front apertures of the geogrids and connecting the wires together throughout the whole height of the abutment.

Table 5 Shaking table test plan

Table & Charming table tool plant				
Abutment	Influencing factors			
No.	Reinforcement spacing, $S_{\nu}(m)$	Tensile strength, <i>T_f</i> (kN/m)	Tensile Stiffness, J (kN/m)	Reinforcement length, <i>L_r</i> (m)
T1-l	0.10	10	170	0.84
T1-R	0.05	5	80	0.84
T2-L	0.10	10	170	1.08
T2-R	0.05	5	80	0.60

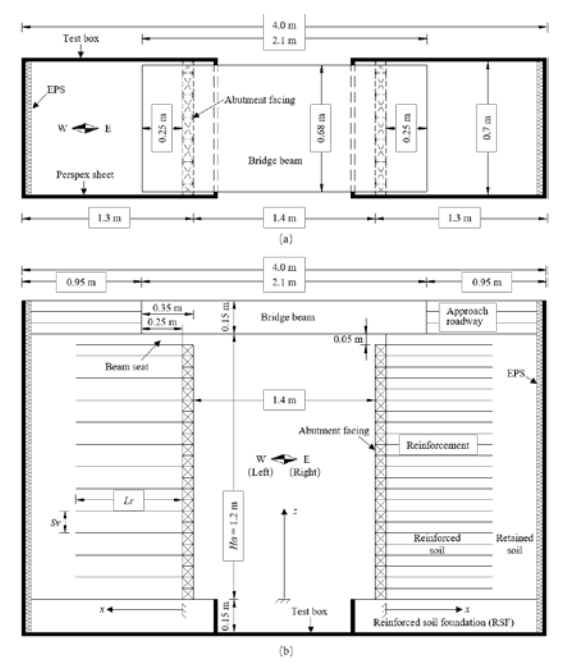


Fig. 19. Test configuration of the model GRS-IBS: (a) top view and (b) cross-sectional view in the longitudinal direction of the bridge beam



Fig. 20. The completed GRS-IBS model before applying the dynamic load

A series of white noises and scaled earthquake motions were applied to the model GRS-IBS in the longitudinal direction of the bridge beam with a short pause of 5 minutes. A total of 21 input motions were applied in this test, as shown in Table 6. The North-South (N-S) component of the earthquake motion recorded by the Japan Meteorological Agency during the Kobe earthquake was used in the test. The input acceleration-time histories for the shaking table model tests were obtained from the original motions according to the similitude relationship. In order to investigate the effects of the magnitudes of peak ground accelerations (PGA) on the GRS-IBS, the acceleration amplitudes of the "motion of similitude" were further scaled to reach different input PGAs, while the frequencies were kept unchanged, as shown in Fig. 21.

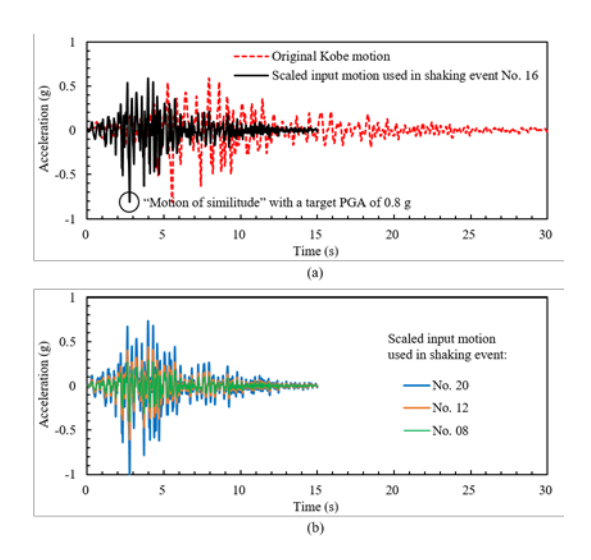


Fig. 21. Time histories of earthquake motions: (a) the original records for the N-S component of the Kobe earthquake versus the scaled input motion used in shaking event No. 16 and (b) scaled input motions used in shaking events No. 8, 12, and 20.

Table 6 Input motions for the shaking test.

Shaki ng event No.	Motion	Input target PGA(g)	Shaking event No.	Motion	Input target PGA(g)
1	White noise	0.05	12	Scaled Kobe	0.6
2	Scaled Kobe	0.1	13	White noise	0.05
3	White noise	0.05	14	Scaled Kobe	0.7
4	Scaled Kobe	0.2	15	White noise	0.05
5	White noise	0.05	16	Scaled Kobe	0.8
6	Scaled Kobe	0.3	17	White noise	0.05
7	White noise	0.05	18	Scaled Kobe White noise Scaled Kobe White noise	0.9
8	Scaled Kobe	0.4	19		0.05
9	White noise	0.05	20		1.0
10	Scaled Kobe	0.5	21		0.05
11	White noise	0.05			

5.2 Test results

Fig. 22 shows the deformation characteristics of T1 after the completion of the shaking test. It can be seen that although there existed lateral facing displacement and differential settlement between the approach roadway and the bridge beam on both sides of GRS abutments, the GRS-IBS showed good stability and did not experience obvious structure failure after applied seismic action with a peak acceleration of 1g, indicating that the GRS-IBS had excellent seismic

performance. In addition, comparing the seismic response and residual deformation characteristics between T1 and T2, it was found that the effect of reinforcement length on the seismic performance of GRS abutments was not significant when reinforcement length exceeded 0.5*H*. Therefore, the results of T1 were mainly analyzed by investigating the effects of different combinations of reinforcement stiffness and spacing on the seismic performance of the whole GRS-IBS.



Fig. 22. Photos of the left and right GRS abutments after the completion of the shaking test (T1)

Fig. 23 shows the distributions of the peak acceleration amplification coefficients along the abutment height at the abutment facing and the reinforced soil zone. The peak acceleration amplification coefficient was defined as the ratio of the measured peak acceleration amplitude at a specific height to the measured PGA. For the left GRS abutment with reinforcement spacing of 0.1 m and reinforcement stiffness of 170 kN/m, the peak acceleration amplification coefficient decreased significantly with the increasing input target PGA. However, for the right GRS abutment with reinforcement spacing of 0.05 m and reinforcement stiffness of 80 kN/m, the peak acceleration amplification coefficients did not have a significant change with the increasing input target PGA. This indicated that the reinforcement spacing plays an important role in minimizing the seismic effect on the GRS abutment under strong earthquake motions than the reinforcement stiffness. Therefore, instead of increasing the reinforcement stiffness, reducing the reinforcement spacing was more effective in enhancing the earthquake resistance of the GRS structure in terms of the acceleration responses. In addition, the peak acceleration amplification coefficients at the abutment facing were smaller than those in the reinforced soil zone.

Fig. 23 also indicated that compared to the shaking table tests of a single GRS abutment (Helwany et al., 2012; Zheng et al., 2019), the existence of the bridge beam could influence the

distribution of the peak acceleration amplitudes near the top of both GRS abutments. The seismic inertial forces applied on both left and right GRS abutments interacted with each other through the bridge beam. This force interaction generated close peak acceleration amplitudes between the two abutments near the bridge beam, such as the abutment facing. However, due to the relatively far away from the bridge beam, the retained soil zone was not significantly influenced by the bridge beam, resulting in different peak acceleration amplitudes in the retained soil zone between the two GRS abutments.

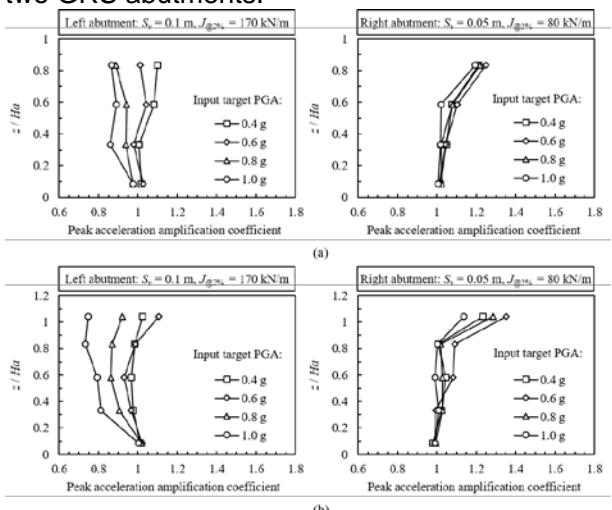


Fig. 23. Distributions of peak acceleration amplification coefficients along the height of the GRS abutment at: (a) abutment facing and (b) reinforced soil zone.

Fig. 24 shows the distribution of modified lateral facing displacements along the elevation of the GRS abutments induced by earthquake motions. The lateral facing displacements for both the right and left GRS abutments showed similar profiles the maximum and minimum displacements happening near the top and bottom of the abutment, respectively. However, smaller lateral facing displacements were found in the right GRS abutment than those in the left abutment. which was consistent with the observations from Fig. 23, indicating that reducing the reinforcement spacing was beneficial for controlling the deformation induced by earthquake motions while the ratio of reinforcement stiffness to reinforcement spacing was kept the same.

Test results also indicated that a significant increase in vertical soil stress was found in the GRS abutment, even though only horizontal seismic motions were applied in the tests, as shown in Fig. 25. Therefore, more attention should be paid to the bearing capacity of the GRS abutment and the underlying foundation when designing the seismic resistance of GRS-IBS structures.

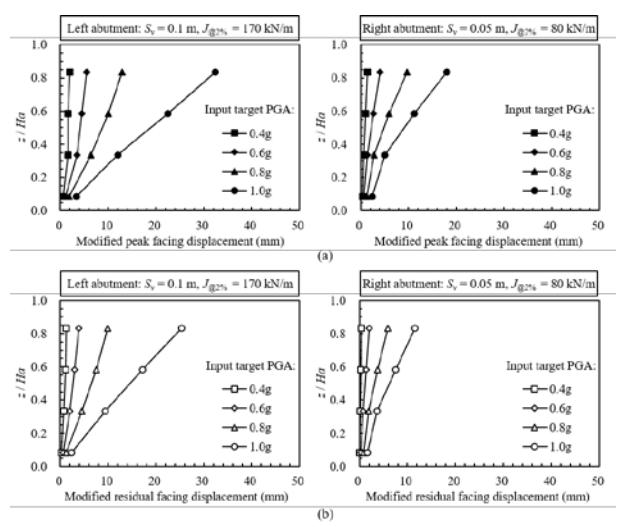


Fig. 24. Distribution of modified lateral facing displacements along the height of the GRS abutments induced by earthquake motions: (a) peak lateral facing displacements and (b) residual lateral facing displacements.

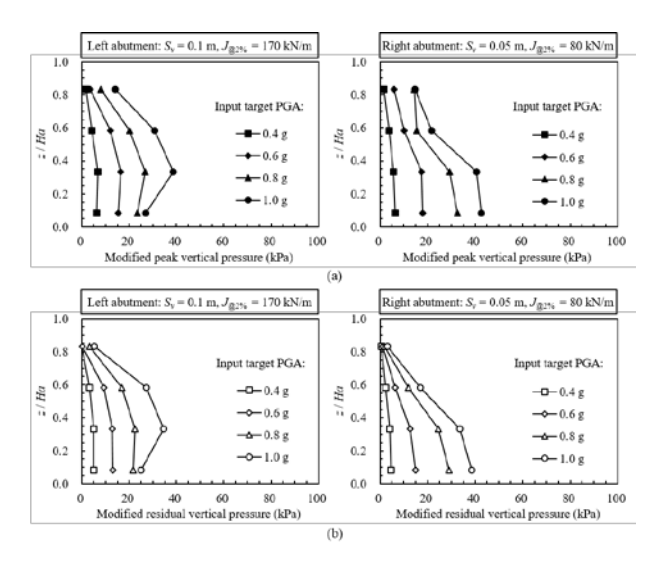


Fig. 25. Distribution of modified vertical stresses in the backfill soil under the center of the beam seat along the height of the GRS abutments induced by earthquake motions: (a) peak vertical stress and (b) residual vertical stress.

6 APPLICATIONS OF THE GRS-IBS IN CHINA

The GRS-IBS has gained increasing global adoption, particularly in the United States, owing to its advantages such as reduced construction cost, environmental friendliness, and effectiveness in eliminating bumps at the end of bridges (Adams et al, 2007; Warren et al., 2010; Mohamed et al., 2011; Lenart et al., 2016; Saghebfar et al., 2017; Jeffrey, 2020). In China, researchers and engineers have greatly developed this new type of technology through continuous systematic research and practical exploration of GRS

abutments or GRS-IBS. To date, four major cases of the GRS abutment or GRS-IBS have been constructed compliant with FHWA guidelines across four distinct provinces. Currently, three projects **GRS-IBS** additional are under construction in Anhui Province. This section provides a detailed case study of the Tongyue Overpass Bridge in Tongcheng City, Anhui Province. The original design of this project was a three-span overpass bridge using a traditional pile foundation to support the bridge load. After a comprehensive technical demonstration research by engineers, the project was significantly optimized. Engineers ultimately selected this project as a pilot initiative to advance GRS-IBS technology while controlling costs. Therefore, the original design of the three-span pile-supported bridge was replaced by a single-span GRS-IBS. Two GRS abutments were used instead of pier abutments at both ends of the bridge beam according to the geological conditions of the bridge site and the functional requirements of the overpass. Post-implementation analysis indicated that the GRS-IBS design achieved a 26% reduction in construction costs compared to the original design of the three-span pile-supported bridge.

The single-span bridge had a total length of 34.4 m with two GRS abutments located at both ends. Considering the self-weight of the girder and the traffic load, the beam seat width and the setback distance were 2.2m and 0.6m, following the FHWA design guidelines (Adams and Nicks, 2018). The height of the left and right GRS abutments was 6.8 m and 6.1 m, respectively, and the beam seat with a length of 12.5 m was cast directly on top of the GRS abutment. The front wall facing and the two wing walls of each GRS abutment were vertical. Fig. 26 shows the geometry of the GRS-IBS. A geological survey showed that the bottom of the excavated GRS abutment was located on the stratum of moderately weathered gravel with a bearing capacity greater than 500 kPa, which could fully meet the requirement of the bearing capacity of the foundation. Therefore, the GRS abutment was directly constructed on the moderately weathered gravel layer without a reinforced soil foundation (RSF). The reinforcement vertical spacing between reinforcement layers of GRS was 0.2 m. Secondary reinforcement was placed within a depth of 1.0 m underneath the beam seat, with a reinforcement spacing of 0.1 m. The base width of each abutment was 2.5 m, and the abutment was constructed layer by layer according to the 1:1 cut slope.

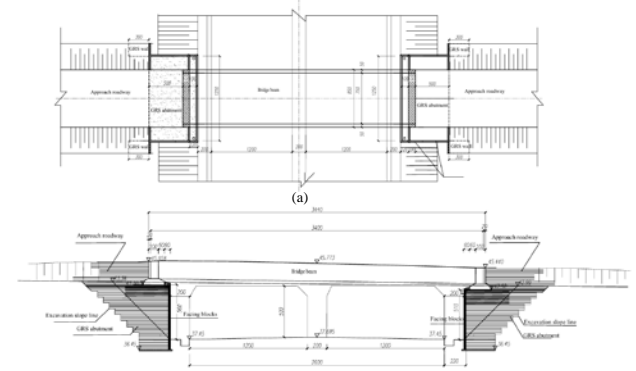


Fig.26. Design of the GRS-IBS: (a) top view; (b) front view

In this project, graded crushed stone with a maximum particle size of 25.4 mm was used as the backfill soil for the GRS abutments and the approach roadway, and the fine content was less than 12% according to the FHWA guidelines (Adams and Nicks, 2018). A polypropylene (PP) geotextile was selected reinforcement material for this project. According to the wide-width tensile tests, the ultimate tensile strength for the selected PP woven geotextile was 100 kN/m in the machine direction and 90 kN/m in the cross-machine direction, respectively. The abutment facing of the GRS abutments was composed of modular blocks with dimensions of $0.4 \text{ m (length)} \times 0.2 \text{ m (width)} \times 0.2 \text{ m (height)}$. The geotextiles were directly placed between two layers of blocks without any fixture, except for the top four layers which were mechanically connected into a whole.

Due to the fact that the GRS abutment was directly located in the moderately weathered gravel with high bearing capacity. construction stages of the GRS-IBS included the GRS abutments, beam seat, bridge beam, and integrated approach. The traditional reinforced soil foundation was not included. For the construction of the GRS abutments, the sequence of each layer followed the placement of the blocks, backfill soil compaction, and the placement of the geotextiles. During the compaction process, two different compactors were used to compact the backfill soil to a minimum relative compaction of 96%. The backfill near the facing was compacted through a smaller plate compactor, while a roller compactor was used for the backfill soil further away from the facing. Additionally, temporary support was used before the front-facing and the wing walls to ensure the facing remained vertical during the compaction process and was removed after construction of the GRS abutment. For the top four layers, hollow modular blocks were used to mechanically connect with the geotextiles by inserting steel bars into the hollow and pouring concrete to enhance the local stiffness of the abutment facing.

The construction of these two GRS abutments began on September 24, 2022, and was completed on October 26, 2022. After the construction of the GRS abutment, the beam seat with steel-reinforced concrete was cast on-site. The steel beam and the integral approach were constructed after the strength of the beam seat concrete reached the design requirements. The whole project was completed on December 29, 2022, and officially opened to traffic on April 1, 2023. Fig. 27 shows some construction processes of this project. Fig.28 shows the completed final GRS-IBS.



Fig. 27 Construction of the GRS-IBS



Fig. 28 Completed Tongyue overpass GRS-IBS

After construction of the GRS abutments, performance monitoring was conducted on the left abutment, and the monitoring plan is shown in Fig. 29. The settlement at the top and bottom of the abutment, and the lateral facing displacement were measured with different pressure settlement gauges and horizontal array displacement gauges, respectively. The performance monitoring period was planned to be conducted for 3 years. In this monitoring system, the sensors were equipped collection capabilities, automatic data enabling remote monitoring through a cloud platform. Real-time data analysis and early warning alerts could be performed through a client-side interface. After 15 months of being open to traffic (7/17/2024), the measured maximum settlement was 14.4 mm occurred underneath the beam seat. The settlement at the foundation was 4.9 mm, indicating the compressive value of the GRS abutment was 9.5 mm. Therefore, the actual vertical strain of the GRS abutment was 0.14%. The maximum lateral facing displacement was 17.6 mm, which was found at a height of 5 m from the bottom. The corresponding lateral strain was 0.63%. Therefore, the deformation of the GRS abutment complied with the requirements of the FHWA guidelines. Based on the current monitoring data, the lateral facing displacement after opening to traffic of the abutment at 15 months and 20 months was basically consistent. Combined with observations on-site, it could be concluded that the GRS abutment was performing very well, and the GRS-IBS was in good service condition.

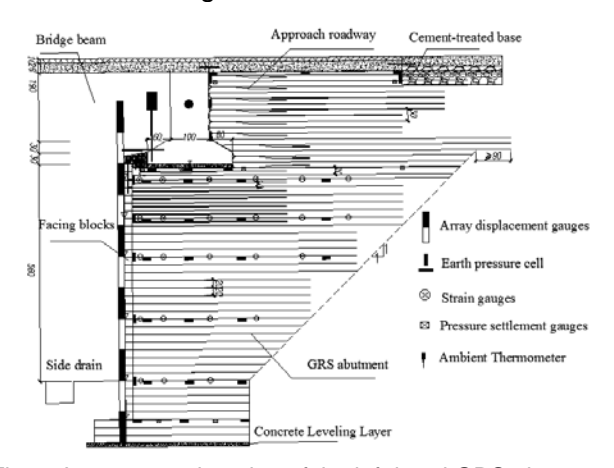


Fig.29 Instrumentation plan of the left-hand GRS abutment

7 CONCLUSIONS

This paper systematically discusses the compressive strength of geosynthetics reinforced soil (GRS) masses, the ultimate bearing capacity of **GRS** abutments, and deformation characteristics under service conditions of GRS abutments, and their corresponding analytical methods. Furthermore, the seismic performance of the geosynthetics reinforced soil-integrated bridge systems (GRS-IBS) was evaluated through two scaled whole GRS-IBS shaking table tests. A representative case study of GRS-IBS in China was also analyzed to demonstrate practical applications. The principal findings are summarized as follows.

- (1) The compressive strength of GRS mass was further investigated through a series of plane-strain tests, considering sand as backfill soil. Building on the experimental results, a semi-empirical method was developed and verified to predict the compressive strength of the GRS mass.
- (2) Five centrifuge model tests of the GRS abutments indicated that the GRS abutment had

high ultimate bearing capacity, and the ultimate bearing capacity was closely related to the setback distance and beam seat width. The failure surface of the GRS abutment was observed from the tests developed from the rear edge of the beam seat, and extended downward at a certain angle to the connection between the facing block and the reinforcements.

- (3) The current calculation method for the ultimate bearing capacity of the GRS abutment did not take into account the abutment design elements. An improved method was proposed based on the limit equilibrium method and verified through the centrifuge model test results. Compared to the current method, this improved method can significantly improve the accuracy of the ultimate bearing capacity calculation.
- (4) The relationship between the maximum lateral facing displacement and the maximum settlement at the top of the abutment was found to be linear under service load conditions, and this relationship was correlated with the setback distance and beam seat width. Furthermore, an improved semi-empirical method to describe the relationship between the maximum lateral facing displacements and the maximum settlements at the top of the abutments was proposed and verified.
- (5) Shaking table tests indicated that the GRS-IBS had excellent seismic performance and could maintain stability under a strong earthquake acceleration. It should be noted that the existence of the bridge beam could influence the distribution of the peak acceleration amplitudes near the top of both GRS abutments.
- (6) The GRS-IBS has been greatly developed and promoted in China, with an increasing number of engineering projects being designed and constructed. At present, the GRS abutments are still a research hotspot in GRS structures. In the future, the application of advanced materials and monitoring technology, artificial intelligence, and other emerging technologies will further promote the development of GRS abutments and GRS-IBS towards a more complete stage.

ACKNOWLEDGEMENTS

This study was supported by the National Natural Science Foundation of China (Grant No. 41772284), the Key Research and Development Project of Chinese Ministry of Science and Technology (Grant No. 2016YFE0105800), and the Key Science and Technology Projects of Anhui Province in Transportation Industry (Grant No. 2022KJQD008). The authors are grateful for their support. Ms. Haoyu Li and Mr. Sheng Zhang from Anhui Transport Consulting & Design Institute Co.,

Ltd. assisted in the Tongyue overpass GRS-IBS. Their assistance in the application of the GRS-IBS is greatly appreciated. Finally, the authors would like to acknowledge Prof. Fumio Tatsuoka for his outstanding contributions to the development of geosynthetics in the world.

REFERENCES

- Abu-Farsakh, M., Ardah, A., Voyiadjis, G., 2018. 3D Finite element analysis of the geosynthetic reinforced soil-integrated bridge system (GRS-IBS) under different loading conditions. Transp. Geotech 15, 70–83.
- Adams, M.T., Schlatter, W., Stabile, T., 2007a. Geosynthetic reinforced soil integrated abutments at the bowman road bridge in Defiance County, Ohio. In: Proc., Geo-Denver 2007. American Society of Civil Engineers, Denver, Colo, 1192 129.
- Adams, M.T., Ketchart, K., Wu, J.T.H., 2007b. Mini Pier Experiments: Geosynthetic Reinforcement Spacing and Strength as Related to Performance. Geosynthetics in Reinforcement and Hydraulic Applications. Geotechnical Special Publication, ASCE, Reston, VA 165, Geo-Denver 2007.
- Adams, M., Nicks, J., Stabile, T., Wu, J., Schlatter, W. & Hartmann, J. 2011. Geosynthetic Reinforced Soil Integrated Bridge System Interim Implementation Guide, FHWA-HRT-11-026. U.S. DOT, Washington, DC, USA.
- Adams, M., Nicks, J., 2018. Design and Construction Guidelines for Geosynthetic Reinforced Soil Abutments and Integrated Bridge Systems. the US Federal Highway Administration, McLean, VA, USA Report No., FHWA-HRT-17-080.
- Ambauen, S., Leshchinsky, B., Xie, Y., Rayamajhi, D., 2015. Service-state behavior of reinforced soil walls supporting spread footings: a parametric study using finite element analysis. Geosynth. Int. 23 (3), 156–170.
- Askari, M., Razeghi, H.R., Mamaghanian, J., 2021. Numerical study of geosynthetic reinforced soil bridge abutment performance under static and seismic loading considering effects of bridge deck. Geotext. Geomembranes 49, 1339–1354.
- Berg, R. R., Christopher, B. R., Samtani, N. 2009. Design and Construction of Mechanically Stabilized Earth Walls and Reinforced Soil Slopes – Volume I, FHWA-NHI-10-024. Department of Transportation, McLean. VA. USA.
- Elton, D.J., Patawaran, M.A.B., 2004. Mechanically stabilized earth reinforcement tensile strength from tests of geotextile-reinforced soil. Transport. Res. Rec. J. Transport. Res. Board 1868, 81–88.
- Han, J., Jiang, Y., Xu, C., 2018. Recent advances in geosynthetic-reinforced retaining walls for highway applications. Front. Struct. Civ. Eng. 12 (2), 239–247.
- Hatami, K., Boutin, J., 2021. Influence of backfill type on the load-bearing performance of GRS bridge abutments. Geosynth. Int. 29 (5), 506–519.
- Helwany, S.M.B., Wu, J.T.H., Kitsabunnarat, A., 2007. Simulating the behavior of GRS bridge abutments. J. Geotech. Geoenviron. Eng. 133 (10), 1229–1240.
- Helwany, S.M.B., Wu, J.T.H., Meinholz, P., 2012. Seismic Design of Geosynthetic Reinforced Soil Bridge Abutments with Modular Block Facing. NCHRP Web-Only Document 187. Transportation Research Board, Washington, DC, USA.
- Jeffrey, A.S.J., 2020. Implementation of Geosynthetic

- Reinforced Soil Integrated Bridge System (GRS-IBS) Technology in Alabama. Auburn University, USA.
- Kakrasul, J.I., Han, J., Rahmaninezhad, S.M., 2020. Load-deformation behavior of geosynthetic-reinforced retaining walls with limited fill space under static footing loading. Transp. Infrastruct. Geotech. 7 (3), 309–331.
- Khosrojerdi, M., Xiao, M., Qiu, T., Nicks, J., 2020. Prediction equations for estimating maximum lateral displacement and settlement of geosynthetic reinforced soil abutments. Comput. Geotech. 125, 103622.
- Lenart, S., Kralj, M., Medved, P.S., Suler, J., 2016. Design and construction of the first GRS integrated bridge with FHR facings in Europe. Transp. Geotech 8, 26–34.
- Leshchinsky, B. 2014. Limit Analysis Optimization of Design Factors for Mechanically Stabilized Earth Wall-Supported Footings. Transp. Infrastruct. Geotech. 1, 111–128.
- Mohamed, K., Abouzakhm, M., Elias, M., 2011. Applications and performance of geosynthetic-reinforced soil abutments on soft subsurface soil conditions. Transport. Res. Rec. 2212, 74–81.
- Mirmoradi, S.H., Ehrlich, M., 2018. Numerical simulation of compaction-induced stress for the analysis of RS walls under working conditions. J. Geotextile Geomembr. 46, 354–365.
- Nicks, J.E., Adams, M., Ooi, P., Stabile, T., 2013. Geosynthetic Reinforced Soil Performance Testing—Axial Load Deformation Relationships. FHWA-HRT-13-066.
- Nicks, J.E., Esmaili, D., Adams, M.T., 2016. Deformations of geosynthetic reinforced soil under bridge service loads. Geotext. Geomembranes 44, 641–653.
- Palmeira, E.M., 2009. Soil-geosynthetic interaction: modelling and analysis. Geo text. Geomembr. 27 (5), 368e390.
- Pham, T.Q., 2009. Investigating Composite Behavior of Geosynthetic Reinforced Soil Mass. Ph.D. dissertation. University of Colorado, Denver.
- Rahmaninezhad, S.M., 2019. Geosynthetic Reinforced Retaining Walls with Flexible Facing under Footing Loading. Ph.D. Dissertation, Civil, Environmental and Architectural Engineering Department, Lawrence, KS, USA. The University of Kansas.
- Ruiken, A., Ziegler, M., Vollmert, L., Hoehny, S., 2011. Investigation of the compound behavior of geogrid reinforced soil. Proceedings of the 15th European Conference on Soil Mechanics and Geotechnical Engineering. Athens, Greece, 1043-1048.
- Saghebfar, M., Abu-Farsakh, M., Ardah, A., Chen, Q., 2017. Performance monitoring of geosynthetic reinforced soil integrated bridge system (GRS-IBS) in Louisiana. Geotext. Geomembranes 45 (2), 34–47.
- Shen, P., Han, J., Zornberg, J.G., Morsy, A.M., Leshchinsky, D., Tanyu, B.F., Xu, C., 2019. Two and three-dimensional numerical analyses of geosynthetic-reinforced soil (GRS) piers. Geotext. Geomembranes 47 (3), 352–368.
- Shen, P., Han, J., Zornberg, J., Tanyu, B.F., Christopher, B.R., Leshchinsky, D., 2020. Responses of geosynthetic-reinforced soil (GRS) abutments under bridge slab loading: numerical investigation. Comput. Geotech. 123, 103566.
- Talebi, M., 2016. Analysis of the Field Behavior of a Geosynthetic Reinforced Soil Integrated Bridge System during Construction and Operation. The University of Delaware, DE, USA.

- Wang, Q., Xu, C., Shen, P., Li, G., Zhao, C., 2024 Experimental and Theoretical Studies on Deformation Characteristics of Geosynthetic-Reinforced Soil (GRS) Abutments Induced by Vertical Loads. Geotext. Geomembranes. 52(5): 925-940.
- Warren, K., Schlatter, W., Adams, M., Stabile, T., LeGrand, D., 2010. Preliminary results for a GRS integrated bridge system supporting a large single span bridge. Earth Retention Conference, Bellevue, Wash., 6122619
- Wu, J.H., Pham, T.Q., Adams, M.T., 2013. Composite Behavior of Geosynthetic Reinforced Soil Mass. Final Report, FHWA-HRT-10-077. Federal Highway Administration, McLean, VA.
- Wu, J.T.H., Pham, T.Q., 2013. Load-carrying capacity and required reinforcement strength of closely spaced soil-geosynthetic composites. J. Geotech. Geoenviron. Eng. 139 (9), 1468–1476.
- Wu, J., Lee, K., Pham, T., 2006. Allowable bearing pressures of bridge sills on GRS abutments with flexible facing. J. Geotech. Geoenviron. Eng. 132 (7), 830–841.
- Xiao, C., Han, J., Zhang, Z., 2016. Experimental study on performance of geosynthetic-reinforced soil model walls on rigid foundations subjected to static footing loading. Geotext. Geomembranes, 44(1), 81–94.
- Xu, C., Liang, C., Shen, P., 2019. Experimental and theoretical studies on the ultimate bearing capacity of geogrid-reinforced sand. Geotext. Geomembranes 47 (3), 417–428.
- Xu, C., Luo, M., Shen, P., Han, J., Ren, F., 2020. Seismic performance of a whole geosynthetic reinforced

- soil-integrated bridge system (GRS-IBS) in shaking table test. Geotext. Geomembranes 48, 315-330.
- Yang, Z., 1972. Strength and Deformation Characteristics of Reinforced Sand. Ph.D. dissertation. University of California, Los Angeles.
- Zhang, X., Xu, C., Wang, Q., Wu, W., 2020. Load test study on bearing characteristics of reinforced soil abutment. Rock Soil Mech. 41(12):4027–4034. (In CHINESE)
- Zheng, Y., Fox, P.J., 2016. Numerical investigation of geosynthetic-reinforced soil bridge abutments under static loading. J. Geotech. Geoenviron. Eng. 142 (5), 04016004.
- Zheng, Y., Fox, P.J., 2017. Numerical investigation of the geosynthetic reinforced soil integrated bridge system under static loading. J. Geotech. Geoenviron. Eng. 143 (6), 04017008.
- Zheng, Y., Fox, P.J., McCartney, J.S., 2018. Numerical simulation of deformation and failure behavior of geosynthetic reinforced soil bridge abutments. J. Geotech. Geoenviron. Eng. 144 (7), 04018037.
- Zheng, Y., Fox, P.J., Shing, P.B., McCartney, J.S., 2019a. Physical model tests of half-scale geosynthetic reinforced soil bridge abutments. I: static loading. J. Geotech. Geoenviron. Eng. 145 (11), 04019094.
- Zheng, Y., McCartney, J.S., Shing, P.B., Fox, P.J., 2019b. Physical model tests of half-scale geosynthetic reinforced soil bridge abutments. II: dynamic loading. J. Geotech. Geoenviron. Eng. 145 (11), 04019095.